Supporting Information

SUPPLEMENTARY NOTE 1: DETERMINATION OF THE MAGNETIZATION MAP FROM THE SCANNING NV CENTER IMAGE

The reconstruction of the magnetization is performed using a machine learning approach (manuscript in preparation). This approach takes the magnetic field image from the NV measurement and generates a mapping to the source, in this case the magnetization of the material. The machine learning loss function is then generated by forward propagating the reconstructed magnetization back into a magnetic field image, which is compared to the original magnetic image. This approach ensures that the reconstructed magnetization image is a valid solution to the magnetic field image that was measured.

For the reconstruction shown in Fig. 1B in the main text, we assumed that the local magnetization was oriented along either the $[1\bar{1}0]$ or $[\bar{1}10]$ direction, consistent with the magnetization hysteresis measurements in Fig. 1A. The correlation between the magnetization map and the stray-magnetic-field map is perhaps not obvious by eye, because a strong magnetic stray field is produced only at domain edges that are perpendicular to the direction of magnetization, not the parallel edges. It is for this reason that the orientation of the stripe-like features in the stray-field map is different than in the magnetization map. As a test, we have also explored the results of the reconstruction algorithm assuming that the local magnetization is oriented along the [010] or $[0\bar{1}0]$ directions, along [110] or $[\bar{1}\bar{1}0]$, or along [100] or $[\bar{1}00]$ (see Fig. S1), but these assumptions were not able to reproduce the measured stray-field maps with the same low error as the result in Fig. 1B in the main text.

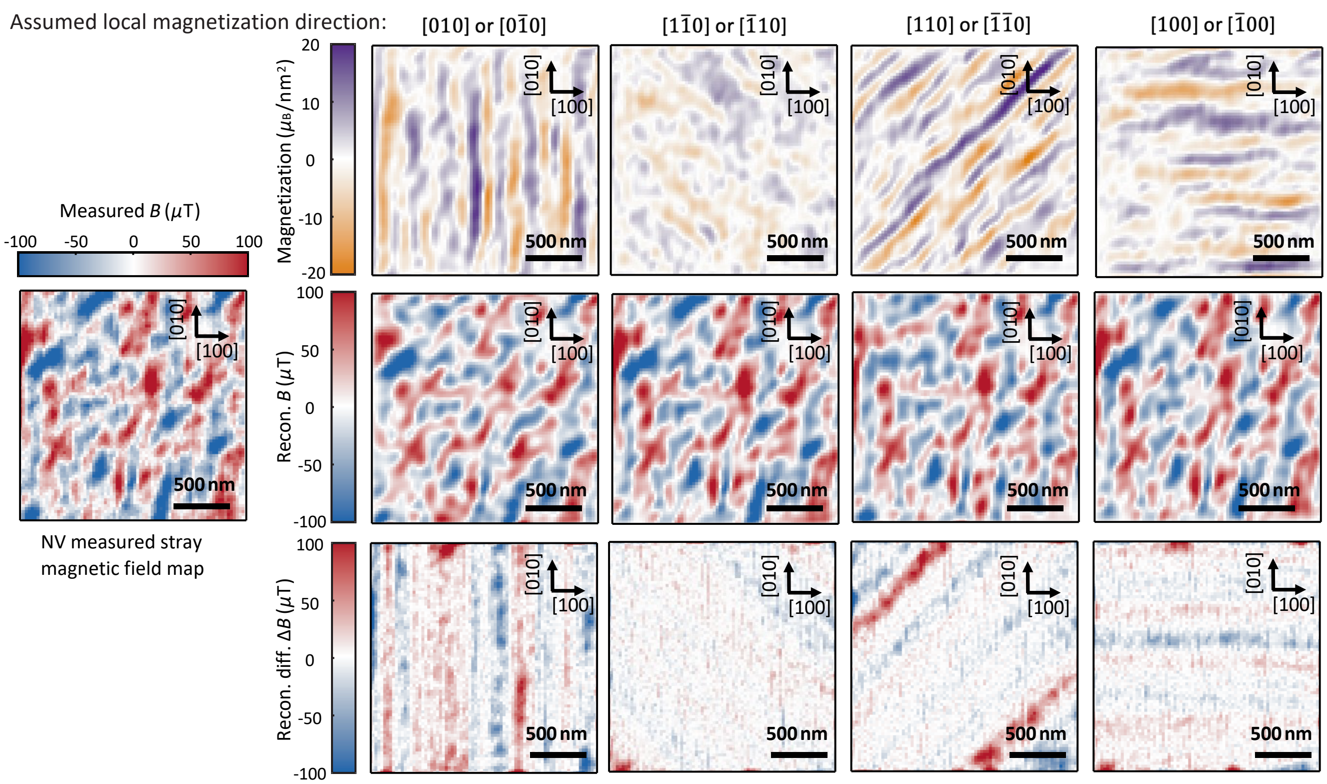

FIG. S1. Comparison of the magnetization reconstruction assuming different local magnetization directions. The far left panel is the magnetic field measured by the NV center. The top row is the magnetization reconstruction by the machine learning algorithm with an assumed local magnetization direction along [010] or $[0\bar{1}0]$, along $[1\bar{1}0]$ or $[\bar{1}10]$, along [110] or $[\bar{1}\bar{1}0]$, or along [100] or $[\bar{1}00]$ (from left to right). The middle row is the reconstructed magnetic field from the magnetization above it. The bottom row is the difference between the reconstructed magnetic field and the measured magnetic field.

SUPPLEMENTARY NOTE 2: MICROMAGNETIC SIMULATIONS

The micromagnetic simulations are performed using the open-source software MuMax3 [1]. A 2D system with 1000 $\times$ 1000 discretized cells is considered, and the size of each cell is 2 nm $\times$ 2 nm, which is significantly smaller than the magnetic exchange length of the MAFO film, $l_{ex} = \sqrt{A_{ex}/0.5\mu_0 M_s^2} \approx 20$ nm. In this formula, the saturation magnetization $M_s = 9.549 \times 10^4$ A/m is from our own measurements; the exchange constant $A_{ex} = 2.22 \times 10^{-12}$ J/m is estimated based on the Curie temperature and the lattice parameters of MAFO [2, 3] and is consistent with typical values for spinel ferrites (for example, A_{ex} for cobalt ferrites is 4×10^{-12} J/m [4]). According to a previous study [5], our coherently-strained (001) MAFO thin films grown on (001) $MgAl_2O_4$ substrates have a large easy-plane anisotropy within the x-y plane, $E_{ep} = K_e m_z^2$ (arising possibly due to the epitaxial strain), as well as a modest biaxial in-plane cubic anisotropy with the crystallographic [110] and [1$\bar{1}$0] directions as the easy axes, $E_{bi} = K_{bi} m_x^2 m_y^2$. Here the anisotropy coefficients $K_e = 6.684 \times 10^4$ J/m^3 and $K_c = 477.5$ J/m^3; and m_i $(i = x, y, z)$ are the components along the three Cartesian axes of the unit vector corresponding to the magnetization (e.g., $+x \parallel [110]$). In the simulation, these two anisotropies are set to exist in all cells of the system. According to the magnetic hysteresis loop in Fig. 1a of the main text, the [1$\bar{1}$0] axis is slightly easier than the [110] axis. To simulate this, we introduce 500 circular pinning sites with a radius of 10 nm that are randomly distributed in the system (see Supplementary Fig. S2a). In each pinning site, there exists an additional uniaxial anisotropy along the [1$\bar{1}$0] axis, $E_{uni} = -K_{uni}(\mathbf{m} \cdot \mathbf{u})^2$, where $\mathbf{u}$ is a unit vector along the [1$\bar{1}$0] axis, with $K_{uni} = 4000$ J/m^3. The magnetization in these pinning sites is randomly initiated (see Supplementary Fig. S2b). The equilibrium magnetic domain pattern is obtained by solving the Landau-Lifshitz-Gilbert (LLG) equation using the fourth-order Runge-Kutta method with a time interval of 10 fs. Periodic boundary conditions are applied along both the x and y axes. The effective magnetic field, which drives the evolution of the initial magnetization distribution to equilibrium, is the sum of magnetic stray field, the Heisenberg exchange coupling field, and the fields arising from the magnetic anisotropies mentioned above. The effective Gilbert damping coefficient α is set to 0.0015 [5].

When we simulate the zero-field magnetic configuration after the application of a saturating magnetic field along the [110] axis, the results indicate the formation of stripe domains oriented along [1$\bar{1}$0] with spins aligned along the same axis and with 180° domains walls separating the domains (see Fig. S3). In this model, the pinning sites work as nucleation sites for the formation of the stripe domains. The results are qualitatively consistent with the NV-center image in Fig. 1b of the main text. The simulated stripe pattern is more ordered than the experimental result, but this may be related to differences in the strength of the pinning sites and the assumption of periodic boundary conditions in the simulation.

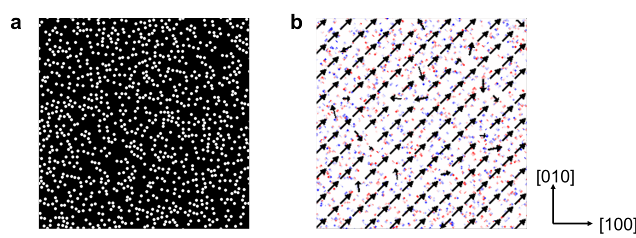

FIG. S2. (a) The location of the 500 randomly distributed pinning sites, which are shown as the white dots and have a radius of 10 nm. (b) The assumed initial magnetization distribution after application of a magnetic field in the [110] direction and then removal of the magnetic field. The magnetization vectors are randomly oriented inside the pinning sites, and are along the [110] direction elsewhere.

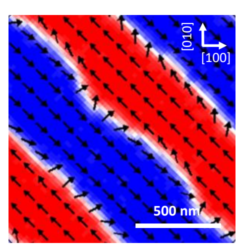

FIG. S3. Domain pattern in the demagnetized state obtained via micromagnetic simulations.

SUPPLEMENTARY NOTE 3: ADDITIONAL FIELD DEPENDENCE DATA

Field Dependence with Different Sweeping Angles

We have measured first-harmonic nonlocal resistances with the external field H_{ext} swept along different in-plane directions ϕ with respect to the Pt wires, as shown in Fig. S4. This figure shows a wider range of field angles and field strengths than Fig. 3 in the main text. At high fields, we observe a slight decrease in the first-harmonic signals due to an increasing Zeeman gap. In the low field regime, $R_{1\omega}$ converges to the same value for a given sample regardless of the angle of the sweeping field. These results confirm the robustness of our observations near zero field.

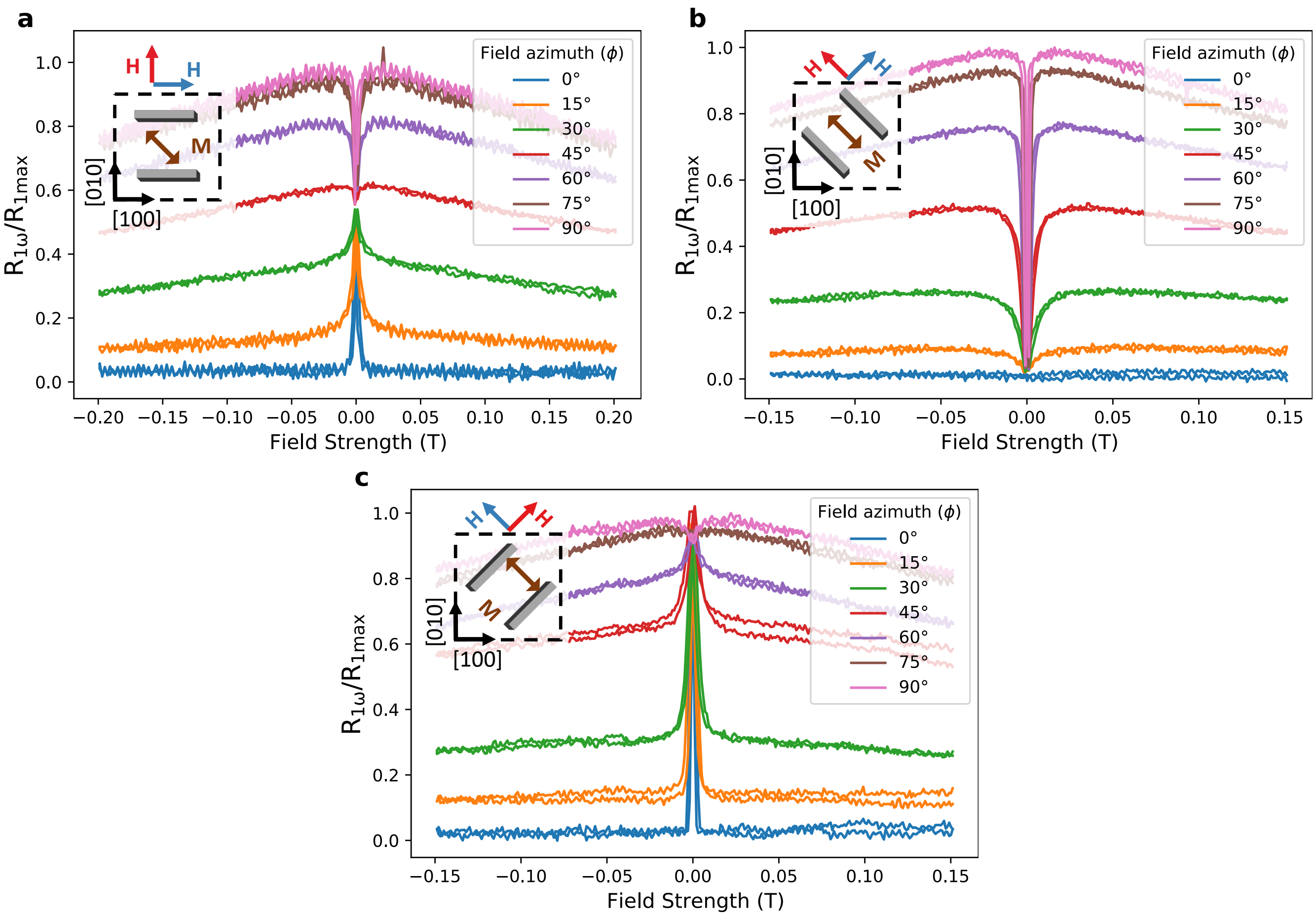

FIG. S4. Normalized first-harmonic nonlocal resistances for for same 6 nm MAFO samples discussed in the main text with a wire separation of 1 μm, with Pt wires along (a) [100], (b) [1$\bar{1}$0], and (c) [110] axes. The lines with different colors correspond to scans with the field H_{ext} swept along different angles ($0^\circ \leq \phi \leq 90^\circ$) with respect to the Pt wires.

SUPPLEMENTARY NOTE 4: CURRENT DEPENDENCE FOR THE FIRST-HARMONIC SIGNAL AT LOW FIELD

To test whether the nonlocal first-harmonic voltage $V_{1\omega}$ near zero magnetic field has any nonlinear current dependence that might arise from current-driven domain wall motion, we performed field sweeps with different alternating current amplitudes on a pair of Pt wires separated by 2.2 μm, which is well above the average size of domains near zero field (hundreds of nanometers). For each current amplitude we plot in Fig. S5 the average of $V_{1\omega}$ measured measured for magnetic-field magnitudes less than 10 mT, with the solid line being the linear fit. We do not observe any deviation from the expected linear dependence.

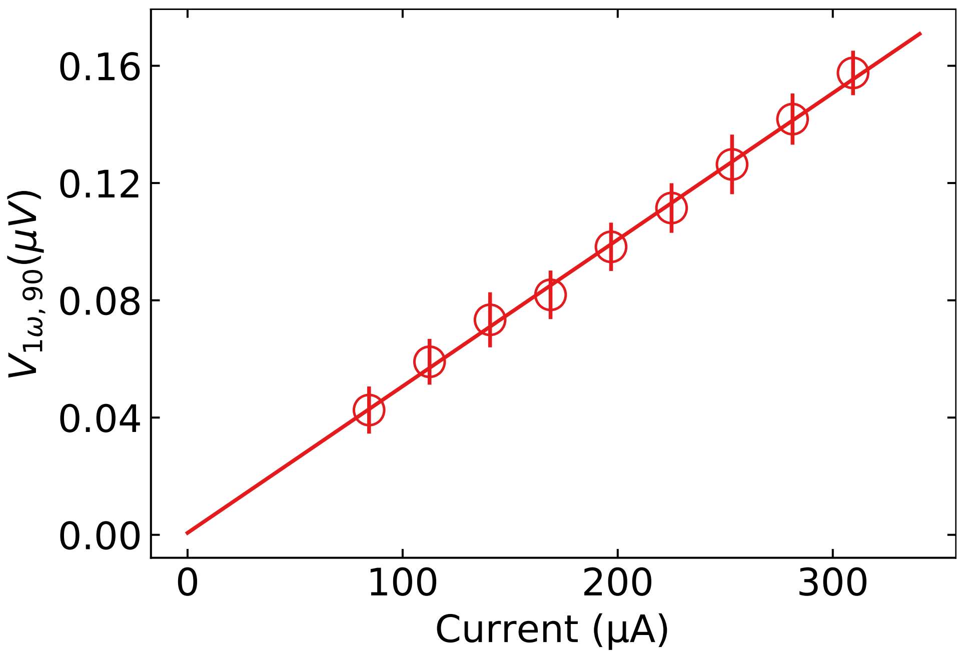

FIG. S5. Current dependence of averaged low-field (<10 mT) first-harmonic voltage for a 6 nm MAFO film with Pt wires along the [110] axes, separated by a distance of 2.2 μm. The external magnetic field is swept perpendicular to the Pt wires.

SUPPLEMENTARY NOTE 5: SCANNING NV CENTER MAGNETOMETRY SETUP

Figure S6 shows the experimental setup of the scanning NV center magnetometry, with the reference angles indicated. The x direction in the figure corresponds to the $[1\bar{1}0]$ crystal axis.

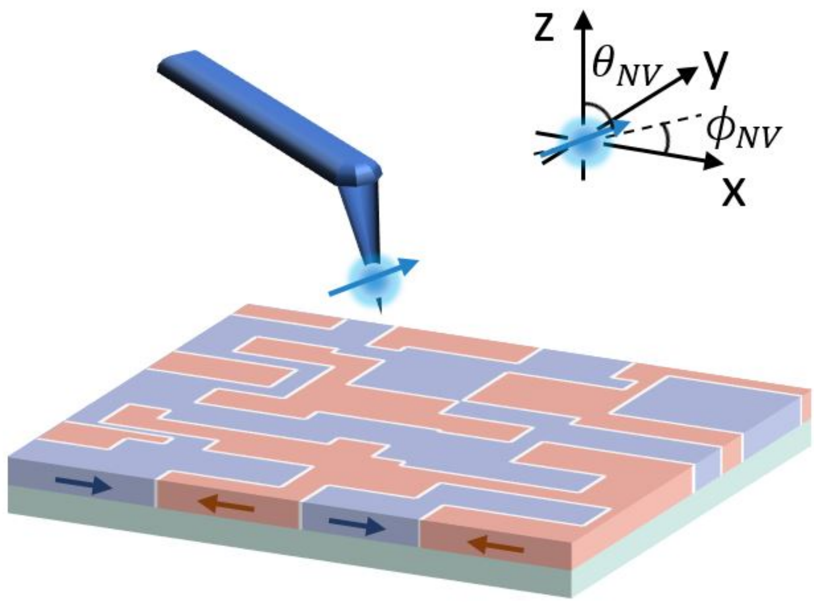

FIG. S6. Schematic drawing of scanning NV center magnetometry

[1] A. Vansteenkiste, J. Leliaert, M. Dvornik, M. Helsen, F. Garcia-Sanchez, and B. Van Waeyenberge, The design and verification of MuMax3, AIP advances **4**, 107133 (2014).
[2] S. C. P. van Kooten, *Ultrafast manipulation of magnetism in a Van der Waals ferromagnet*, Ph.D. thesis, Eindhoven University of Technology (2020).
[3] C. Kittel, Physical theory of ferromagnetic domains, Reviews of modern Physics **21**, 541 (1949).
[4] A. V. Azovtsev and N. A. Pertsev, Dynamical spin phenomena generated by longitudinal elastic waves traversing $CoFe_2O_4$ films and heterostructures, Phys. Rev. B **100**, 224405 (2019).
[5] S. Emori, D. Yi, S. Crossley, J. J. Wisser, P. P. Balakrishnan, B. Khodadadi, P. Shafer, C. Klewe, A. T. N'Diaye, B. T. Urwin, K. Mahalingam, B. M. Howe, H. Y. Hwang, E. Arenholz, and Y. Suzuki, Ultralow damping in nanometer-thick epitaxial spinel ferrite thin films, Nano Letters **18**, 4273 (2018).